# BALLOONING MODES IN AN AXISYMMETRIC MIRROR MACHINE

by

R. A. Close and A. J. Lichtenberg

Memorandum No. UCB/ERL M87/29

15 May 1987

# BALLOONING MODES IN AN AXISYMMETRIC MIRROR MACHINE

by

R. A. Close and A. J. Lichtenberg

Memorandum No. UCB/ERL M87/29

15 May 1987

ELECTRONICS RESEARCH LABORATORY

College of Engineering
University of California, Berkeley
94720

# BALLOONING MODES IN AN AXISYMMETRIC MIRROR MACHINE

by

R. A. Close and A. J. Lichtenberg

Memorandum No. UCB/ERL M87/29

15 May 1987

ELECTRONICS RESEARCH LABORATORY

College of Engineering
University of California, Berkeley
94720

# Ballooning Modes in an Axisymmetric Mirror Machine

R.A. Close and A.J. Lichtenberg
Electronics Research Laboratory
University of California, Berkeley, CA 94720

**Abstract**

High-beta ballooning modes are studied in an axisymmetric multiple mirror which is made average-minimum-B with end cusps. Electric and magnetic field measurements in the plasma characterize the predominant mode as $m = 1$. The ballooning character of the mode is determined by measuring the ratio of the mode amplitude near the device center to that near the cusp, and confirmed by measurement of perturbed perpendicular magnetic fields. Theoretical growth rates are calculated numerically using ideal and resistive MHD equations for the rigid $m = 1$ ballooning mode. We find within experimental error that the $m = 1$ resistive ballooning growth rate scales as $\langle\beta\rangle^{1/2}$ for radially averaged $\langle\beta\rangle \lesssim 0.07$ (on-axis $\beta_0 \lesssim 0.15$), in agreement with theory. The observed growth rates also increase with mirror ratio as expected. Resistive growth rates calculated numerically agree reasonably well with experimental observations assuming a fixed time for growth of the mode.

# 1 Introduction

The experiments discussed in this paper were developed as part of an ongoing study of plasma stability in the Berkeley Multiple Mirror Experiment (MMX) [1], [2]. Previous experiments demonstrated stabilization of a ten-meter multiple mirror to MHD flute interchange modes by the use of linked quadrupole fields to produce an average- minimum-B magnetic well [1],[2]. This configuration was reported to be stable against ballooning modes for $\beta \leq 0.25$ and mirror ratio $R_m \leq 5$ .

Recently attention has been given to axisymmetric mirror systems because of the simplicity of design and construction and favorable radial confinement properties. The experiments described here examine the stability of an axisymmetric multiple mirror terminated with end cusps to provide stabilizing good curvature. Stability is examined over a range of plasma beta ($\beta \lesssim 0.30$), curvature drive ($R_m \lesssim 7$), and system length ($225 \leq L \leq 450$ cm).

Experimental data on MHD ballooning modes is limited, although these modes are believed to have been observed in many experiments. Instabilities driven by rotation in linear theta pinches have been observed to have azimuthal and radial mode numbers $m = 1$ and $n = 0$, respectively [3]. Using finite Larmor radius fluid equations, Freidberg and Pearlstein [4] showed that a rotationally driven $m = 1$, $n = 0$ ballooning mode can be theoretically unstable for any beta and has the lowest threshhold rotation frequency $\Omega_R$ for instability. Such modes should not be confused with the faster curvature-driven modes which constitute our primary observations, but might be observed late in time.

Ideal and resistive MHD ballooning modes were observed by Hatakeyama *et al* [5] in a simple magnetic mirror with a conducting endplate. They observe a standing wave in the mirror cell with azimuthal mode number $m = 2$ which increases in amplitude as $\beta$ increases. The direction of azimuthal propagation changes as $\beta$ approaches $\beta_c$, the critical value for ideal MHD instability. The authors associate this change of rotation with a transition from the resistive to the ideal MHD regime. We observe both directions of azimuthal propagation but are unable to determine any relationship with other plasma parameters.

The ballooning $m = 1$ displacement mode is widely considered the most dangerous for mirror-confined plasmas. Modes with higher azimuthal numbers tend to be stabilized by finite Larmor radius effects (FLR), which take into account the unequal drifting of ions and electrons in the non-uniform electric fields. Kaiser and Pearlstein [6] have shown that FLR should affect the $m = 1$ mode by keeping the displacement radially rigid. Kang [7] has developed ideal and resistive MHD computer codes for the rigid $m = 1$ ballooning mode in the Berkeley Multiple Mirror. The numerical codes are based on the fluid equation of Lee and Catto [8], and include the effects of non-paraxial curvature in the cusp. These codes are used to calculate theoretical growth rates for comparison with experiment.

Ballooning instabilities have been studied in the MMX using the same plasma sources but different magnetic field configurations than considered here [1], [2]. Depending on the configuration, critical $\beta$'s were found, for the onset of ballooning, that vary from 5% for the most unstable configuration to greater than 25% for the standard multiple mirror configuration. The

$m = 1$ azimuthal mode was predominant, with some admixture of $m = 2$ . The experimental results were compared with predictions from ideal MHD theory. The theoretical results generally predicted somewhat higher critical betas for the $m = 1$ mode than those observed. Because of the complicated nature of the magnetic field configuration it was not possible to check the scaling of the growth rate with experimental parameters.

# 2 Experiment

The high-$\beta$ ballooning modes are excited in the MMX using a variable number of cells (see Figure 1). The MMX is described fully in references [2],[9], and [10]. The axisymmetric mirror cells are made average-minimum-B by the use of end cusps, which are formed by using reverse current in ordinary mirror coils. The cusp coils produce a peak field on axis of 3 kG opposite to the 1.5 kG solenoidal field. The mirror ratio is varied up to a mirror ratio $R_m \approx 7$ . Hydrogen plasma is injected from both ends of the axisymmetric mirror configuration through the solenoid and rising mirror and cusp fields using a conical theta pinch and a Marshall gun. The counterstreaming plasmas thermalize to yield $5 \lesssim T_e \lesssim 15$ eV, $n \lesssim 1 \times 10^{15}$ cm$^{-3}$, and on-axis values of $\beta \lesssim 0.30$ . The two-source injection is timed to yield peak plasma density and pressure in the center of the multiple mirror region. We generally observe that, as the plasmas interact, the ion-saturation current ($\sim nT^{1/2}$) peaks about 10 $\mu$sec earlier than the diamagnetic signal ($\langle\beta\rangle \sim p_\perp/B^2$). This is because the plasma flow velocity affects the ion-saturation current collected but the flow energy does not contribute to $\beta$. As the counterstreaming plasmas interact via collisions, the parallel flow

energy becomes isotropic within 10 $\mu$sec. Subsequent $\langle\beta\rangle$ decay times vary from 5-50 $\mu$sec, with high $\langle\beta\rangle$ decaying faster.

In the experiments, the time evolution of plasma $\beta$, radial density profile, and plasma motion are measured for each shot. The electron temperature, flow energy, and electric and magnetic field fluctuations are measured only on selected shots to characterize the plasma behavior. The diagnostics used are electric probes operated in various regimes, magnetic induction probes, and compensated diamagnetic loops.

Our principal diagnostics for monitoring plasma motion are arrays of Langmuir probes which measure ion-saturation current at different locations in the plasma. For a known plasma profile (we fit to a modified Gaussian $\exp\left\{-r^2/r_p^2\right\}$), an array of four probes at 90° intervals provides information about the $m = 1$ and $m = 2$ components of the plasma motion. By using two arrays at the same axial position but at different radii, the plasma radius $r_p$ (for the Gaussian model) can be determined. Using Langmuir probe arrays at different axial positions measures the $z$-dependence of the plasma motion so that flute modes (with amplitude independent of $z$) are distinguished from ballooning modes ($z$-dependent). Our method for measuring plasma displacement, using probes at $r < r_p$, ensures that we observe global plasma motion rather than edge fluctuations which might be associated with drift waves.

The electron temperature was measured on some shots using an array of Langmuir probes with different bias voltages to detect the exponential change of electron current as a function of voltage due to the Boltzmann factor $\exp\left\{e\left(V - \Phi_p\right)/T\right\}$. The measured temperature is typically between

$5 - 15$ eV at the time of peak density and 20 $\mu$sec later is consistently about 5 eV . On the basis of this data, we decided to use $T = 5$ eV for our numerical calculations. We measure values of $\beta \lesssim 0.30$, so the density $n \lesssim 2 \times 10^{15}$ cm$^{-3}$. This is roughly consistent with our peak ion-saturation current measurements ($nT^{1/2}$).

We compare the plasma centroid motion at different axial positions to distinguish between flutelike and ballooning instabilities. The calculation of the centroid position is described in Appendix A . Figure 2 shows centroid motion (1) in a mirror cell and (2) near a cusp. During the first twenty microseconds the plasma centroid in the unstable mirror cell moves a distance on the order of a plasma radius, while the plasma centroid near the cusp is essentially fixed, clearly indicating ballooning motion.

Floating potential measurements, described in Appendix B, are used to calculate an $\mathbf{E} \times \mathbf{B}$ drift velocity which is compared to the velocity obtained from the Langmuir probe array measurements. As shown in Figure 3, the two measurements of plasma motion are in good agreement until the plasma moves far off center, when neither method can be considered reliable. The agreement between these two methods of calculating plasma motion identifies the mode as an $m = 1$ displacement and verifies the perpendicular part of Ohm's law $\mathbf{v} = \mathbf{E} \times \mathbf{B}/B^2$.

The measurements of the perturbed magnetic field are compared to the plasma motion calculated from Langmuir probe measurements in order to determine whether magnetic field line bending is produced by the mode as predicted by ideal MHD theory. Figure 4 shows a comparison of perturbed magnetic field and plasma motion for a flute-unstable plasma, which should

not have any associated magnetic perturbation. Figure 5 compares the perturbed magnetic field and the plasma motion for a plasma stabilized against flutes (ballooning). A good correlation between the magnetic perturbation and the plasma motion is observed, indicating MHD ballooning. However, the magnetic field perturbation decays after $t \approx 50$ $\mu$sec, indicating finite resistivity.

The $m = 1$ displacement $\xi$ is determined using arrays of eight and four Langmuir probes. The driving force of the instability is, in the low-$\beta$ approximation, $(p_\parallel + p_\perp)\nabla B/B$ . We therefore expect the instability to grow while flow energy ($p_\parallel$) is being converted to diamagnetism ($\beta \propto p_\perp$). Theoretically, it is the radially averaged pressure which drives the instability. In principle this average should be taken over the region which moves rigidly as the instability grows. We estimate this region to extend to within 0.5 cm of the wall, so we take the plasma boundary to be $r_b = 4.0$ cm.

We generally observe a peak in $\xi$ within 10 $\mu$sec after the $\beta$ peaks. Afterward the motion becomes quite complicated. We restrict our observations to the 10 $\mu$sec time interval after $\beta$ peaks. Theoretical growth rates are calculated using the peak value of $\beta$.

The total plasma energy is decaying during the time that parallel flow energy is being converted to flow energy. We therefore expect calculated growth rates to be slightly underestimated. Experimental conditions such as initial plasma temperatures above 5 eV or the lack of a steady-state equilibrium may either increase or decrease the actual growth rate of the instability relative to theoretical expectations.

For computing the plasma displacement $\xi$, the plasma radius is measured at the time of peak $\beta$, and assumed to remain fixed thereafter. This assumption reduces noise introduced by distortion of the plasma profile as it moves toward the chamber wall.

# 3 Results

The parameters which we use for comparison with theory are the plasma displacement $\xi$, the radially averaged beta $\langle\beta\rangle$, the ratio of pressure in the central mirror midplane to that in the cusp $p_m/p_c$, the mirror ratio $R_m$, and the number of mirror cells $N_c$ . The experimental values of $\langle\beta\rangle$, $p_m/p_c$, $N_c$, and $R_m$ are used to obtain a theoretical growth rate $\gamma_T$ . The plasma is assumed to be injected with a small but finite initial $m = 1$ displacement $\xi_0$ which grows exponentially (growth rate assumed constant) while $p_\parallel + p_\perp$ is large.

Numerical calculations used for comparison with experiment are performed using ideal and resistive ballooning codes developed by Kang [7]. Because FLR tends to stabililze modes with radial or azimuthal variation, the least stable mode is assumed to be a radially rigid displacement of the plasma (uniform for fixed $z$). The magnetic field line curvature is calculated in the paraxial limit ($\partial B/\partial r \gg \partial B/\partial z$) except in the cusp region, where the paraxial approximation is invalid. A model of the cusp contribution to the curvature drive developed by Kang assumes that the cusp contains a $\beta = 1$ interior surrounded by an adiabatic plasma with constant magnetic field strength and plasma pressure, and then a vacuum field region. The endpoints of the calculation are taken to be where the fieldline with midplane radius of 2.0 cm hits the wall ($r_w = 4.5$ cm) in the cusp region. Floating end conditions $\partial\xi/\partial z = 0$ are used (no line-tying). We assume a uniform temperature of 5 eV and, for the resistive calculation, we use the corresponding resistive decay time $\tau_R = 43\mu$sec. The solenoidal magnetic

field is 1.5 kG, and the mirror ratio is varied up to $R_m \approx 7$ . The theoretical model assumes a Gaussian profile with plasma radius $r_p = 2.5$ cm and a cutoff at $r_b = 4.0$ cm. Wall effects are not included. The plasma pressure is assumed to fall in steps, with a constant ratio at each mirror moving away from the central cell.

For $N_c = 3$, with values of central mirror cell to cusp cell pressure ratio $p_m/p_c < 3$, critical $\beta$ values for onset of ideal ballooning ($\tau_R \rightarrow \infty$) are above experimental limits ($\beta_c > 0.30$ for $R_m \leq 6$). For $N_c = 1$, critical $\beta$ values are $\beta_c > 0.30$ for all $R_m \leq 6$ with $p_m/p_c \leq 10$ . Growth rates for the resistive calculations are plotted as a function of $\beta$ in Figure 6. Resistive growth rates are plotted as a function of $R_m$ in Figure 7.

Numerically calculated growth rates are used for comparison with theoretically observed mode amplitudes. The $m = 1$ displacement $\xi$ is assumed to grow at a constant (or average) rate $\gamma$ for a fixed time $t_0$, so that $\xi = \xi_0 \exp\{\gamma t_0\}$ or equivalently $\ln \xi = \ln \xi_0 + \gamma t_0$ . By finding $\xi_0$ experimentally (the intercept of a plot of $\ln \xi$ versus $\gamma t_0$), we can obtain growth rates from experimental observations of mode amplitude.

The dependence of $\ln \xi \propto \gamma t_0$ on $\langle\beta\rangle^{1/2}$ with $p_m/p_c$ as a parameter is shown in Figure 8. Theoretical curves are drawn for $N_c = 1$, $R_m = 4$, $\ln \xi_0 = -1.45$ . This value of $\xi_0$ was chosen to match the experimental intercept at $\langle\beta\rangle = 0$. A least-squares linear fit gives $\ln \xi = (-1.45 \pm 0.31) + (7.1 \pm 1.2)\ \langle\beta\rangle^{1/2}$ . The exponent of $\langle\beta\rangle$ in the expression $\ln \xi = a + b\langle\beta\rangle^{\alpha}$ was determined to be $\alpha = 0.44 \pm 0.16$, in reasonable agreement with the theoretical expectation $\alpha \approx 0.50$ . The procedure used to obtain this estimate of $\alpha$ is described in Appendix D . Figure 9 shows the scaling of $\ln \xi$

with mirror ratio $R_m$ for $N_c = 1$, $0.068 \leq \langle\beta\rangle \leq 0.108$, and $1.0 \leq p_m/p_c \leq 3.0$ . A theoretical curve with $\langle\beta\rangle = 0.09$, $p_m/p_c = 2.0$, $t_0 = 10$ $\mu$sec, $\ln\xi_0 = -1.0$ is shown for comparison.

Plotting the data points against the theoretical growth rates calculated from $R_m$, $\langle\beta\rangle$, and $1.0 \leq p_m/p_c \leq 3.0$ gives Figure 10, which agrees with theory for $t_0 = 9.1 \pm 1.7$ $\mu$sec. The slope $t_0$ was calculated using weightings determined from estimates of experimental statistical errors.

With $N_c = 3$ (three mirror cells), some shots are observed to have flute-like behavior, classified by large displacement in both the central mirror cell and in the midplane near a cusp ($\xi_c$) such that $\xi_m/\xi_c < 1.5$ . The flute shots are excluded from the following analysis. The plot of $\ln\xi$ versus $\langle\beta\rangle^{1/2}$ for $N_c = 3$, $R_m \geq 3.0$, and $1.0 \leq p_m/p_c \leq 3.0$ is shown in Figure 11 . A least-squares linear fit gives $\ln\xi = (-1.89 \pm 0.53) + (11.0 \pm 3.5)\,\langle\beta\rangle^{1/2}$. Comparing with the single mirror cell case, three cells have slightly higher growth rates and lower offset due to $\xi_0$ . However, one standard deviation variation in either the intercepts or slopes would cause the data to overlap. For three cells, a larger offset would be more in agreement both with theory and with the single cell results. The theoretical curves drawn have $R_m = 4$, $\ln\xi_0 = -1.4$, and $p_m/p_c = 1, 3$. Figure 12 shows a graph of $\ln\xi$ versus $R_m$ for $N_c = 3$, $0.017 \leq \langle\beta\rangle \leq 0.041$, and $1.0 \leq p_m/p_c \leq 4.0$ . A theoretical curve with $\langle\beta\rangle = 0.027$, $p_m/p_c = 2.0$, $t_0 = 10$ $\mu$sec, and $\ln\xi_0 = -1.0$ is drawn for comparison.

Using the experimental parameters to calculate theoretical growth rates, we get Figure 13 for $1.0 \leq p_m/p_c \leq 3.0$. These points agree with theory for $t_0 = 11 \pm 4$ $\mu$sec.

The experimental values for $t_0$ obtained from the slope of $\ln \xi$ versus $\gamma_T$ are in good agreement for $N_c = 1$ and $N_c = 3$, which is expected because radial losses are dominant. Both values of $t_0$ are close to the assumed value of 10 $\mu$sec, justifying the assumption of constant growth rate during the beta peak. Measurement uncertainties can account for a significant part the scatter, implying that the spread in $\xi_0$ is smaller than its average value.

For the one- and three-cell configurations, we looked for a correlation between the direction of azimuthal propagation (sign of $\dot{\theta}$) and other parameters ($\beta$, $p_m/p_c$, $\xi$). Although we observed instances of both $\dot{\theta} > 0$ and $\dot{\theta} < 0$, there did not appear to be a relationship between the sign of $\dot{\theta}$ and the other measured parameters.

# 4 Conclusions

Electromagnetic $m = 1$ ballooning instabilities have been observed in axisymmetric multiple mirrors stabilized by end cusps. The $m = 2$ mode is not observed except in conjunction with $m = 1$, consistent with predictions of finite Larmor radius magnetohydrodynamic theory. The observed mode is a radially global displacement of the plasma satisfying $\mathbf{v} = \mathbf{E} \times \mathbf{B}/B^2$ with $\mathbf{E}$ the measured instability electric field. The magnetic perturbation $\mathbf{B}_\perp$, resulting from magnetic field line bending, is measured and found to be consistent with the observed ballooning. The magnetic perturbation decays faster than the plasma displacement because of finite resistivity. Instabilities are observed at values of $\langle\beta\rangle$ well below the critical value $\langle\beta_c\rangle$ for ideal MHD ballooning. Growth rates are large compared to the resistive decay time $\tau_R$. The experimental results are compared with numerical calculations from a resistive MHD ballooning code.

For a single mirror cell stabilized by end cusps, the natural logarithm of the mode amplitude $\ln\xi$ ($\propto \gamma$) is found to increase with the radially averaged beta $\langle\beta\rangle$ in the central cell. The dependence is $\ln\xi \propto \langle\beta\rangle^{0.44\pm0.16}$, in good agreement with the theoretical expectation $\gamma \sim \langle\beta\rangle^{1/2}$ . Taking the experimentally observed amplitude $\ln\xi \propto \gamma t_0$, where $t_0$ is the time for which the pressure is sufficiently high that the mode is growing, good agreement with theory is obtained for constant $t_0 = 10$ $\mu$sec. This agreement with theory is surprisingly good considering the simplifying assumption of constant growth rate over a fixed time interval.

Experimentally observed mode amplitudes increase with mirror ratio as expected, with weak dependence for $R_m \gtrsim 3$, and with weak dependence

on $p_m/p_c$ . No significant dependence of ballooning growth rate on system length was observed, but flute-like instabilities were often observed with three mirror cells but not with one. This lack of length dependence for ballooning is not surprising since the plasma pressure is usually strongly peaked in the central cell.

The resistive decay time scales like $r_b^2$ ($r_b$ is the radius out to which the mode is rigid), so resistivity is less important in devices with larger plasma radii. The dimensionless quantity $\tau_R\gamma_{\rm MHD}$ gives an indication of the importance of resistivity. In our experiment $\tau_R\gamma_{\rm MHD} \approx 5$ . Since $\tau_R \propto \sigma_\parallel \propto T^{3/2}$ and $\gamma_{\rm MHD} \propto T^{1/2}$, it follows that $\tau_R\gamma_{\rm MHD} \propto T^2$ . This indicates that resistive effects would not be of great importance in high temperature devices. For example, at $T = 50$ eV, $\tau_R\gamma_{\rm MHD} \approx 500$, giving a growth rate at $\beta = 0.1\ \beta_c$ of 10% of the growth rate at $\beta = \beta_c$.

# A Calculation of Plasma Motion

Eight Langmuir probes span two circles of radii $r_1$ and $r_2$ at 90° intervals. The plasma profile is assumed Gaussian in each of two dimensions, with elliptical contour surfaces:

$$n(x,y) = n_0 \exp\left\{-\frac{(x-x_0)^2}{r_x^2} - \frac{(y-y_0)^2}{r_y^2}\right\} \qquad (1)$$

The eight probes in order are positioned at $(x,y)$=$(r_1,0)$,$(0,-r_1)$,$(-r_1,0)$,... $(0,r_2)$. Labelling the probes as in Figure 14, we derive the following:

$$r_x = \left[\frac{2(r_2^2 - r_1^2)}{\ln(i_1 i_3 / i_5 i_7)}\right]^{1/2}$$
$$r_y = \left[\frac{2(r_2^2 - r_1^2)}{\ln(i_2 i_4 / i_6 i_8)}\right]^{1/2} \qquad (2)$$
$$\epsilon = \frac{r_x}{r_y}$$

where $\epsilon$ is the ellipticity, which measures the magnitude of the $m = 2$ mode.

The plasma radius is defined by $r_p^2 = r_x r_y$ . Because non-Gaussian profiles can introduce spurrious ellipticity into the calculation, we set $r_x = r_y = r_p$ to calculate $(x_0, y_0)$. To reduce sensitivity to edge fluctuations, we require that the plasma radius be less than the wall radius ($r_p < r_w$). We use only the inner probes to calculate:

$$x_0 = \frac{r_p^2}{4r_1}\ln\left(\frac{i_1}{i_3}\right)$$
$$y_0 = \frac{r_p^2}{4r_1}\ln\left(\frac{i_4}{i_2}\right) \qquad (3)$$

These calculations are relatively insensitive to errors. A miscalibration of the probes, for example, essentially results in a constant offset of $(x_0, y_0)$. Also, the probes used to measure the centroid motion have $r_l < r_p$, so that only bulk motion on the same scale as the plasma radius is detected (measurements are insensitive to edge fluctuations). Ellipticity ($m = 2$ mode) is only considered important when the plasma displacement ($m = 1$) is

small because non-gaussian profiles make ellipticity measurement inaccurate when the plasma is off center. One drawback of this procedure is the sensitivity to the measured plasma radius, which is not even well-defined if the density profile is not truly Gaussian. In practice, we use the eight-probe array to calculate the plasma radius at the time $t_\beta$ where the plasma $\beta$ peaks. The plasma radius is then assumed to be fixed as the plasma moves, so only the inner four probes are used to calculate $\xi$.

# B Electric Field Determination

We consider two causes of electric fields in the plasma: (1) a radial ambipolar field, and (2) a uniform field which results from charge drifts in the curved magnetic field. The total potential is a superposition of the potentials from each of these effects.

Diffusion in the multiple mirror gives rise to ambipolar potentials in two ways. First, ambipolar diffusion parallel to B produces a positive potential in the plasma due to the faster escape of electrons. Second, ion-ion radial diffusion produces a potential minimum on axis, with a radially inward electric field. Collisions between ions and electrons give rise to radial diffusion, but do not cause charge separation and therefore do not affect the radial potential profile.

In order to justify our assumption of uniform temperature in the plasma, we show that the variations in floating potential in the plasma are due to the existence of real space potential variations. The observed floating potential profiles, in particular the scaling with density, can be explained by the

following model based on ambipolar diffusion. We assume a quasi-static situation ($d/dt \approx 0$). Collisions between electrons and ions are naturally ambipolar and do not give rise to radial electric fields. Radial ion-ion diffusion generates electric fields, and is balanced by electron end loss to preserve quasineutrality. Only these fluxes are considered in determining the electric field. The electron momentum balance equation along $\hat{\mathbf{z}}$ is:

$$-\frac{dp_e}{dz} - enE_z - m_e n \nu_{ei} v_z^e = 0 \tag{4}$$

which yields the electron end flux:

$$\Gamma_z^e = -\frac{en}{m_e \nu_{ei}} E_z - \frac{T}{m_e \nu_{ei}} \frac{dn}{dz} \tag{5}$$

The ion flux due to ion-ion diffusion in an azimuthally symmetric cylidrical plasma is given by [12]:

$$\Gamma_r^i = \frac{3}{8} n r_L^4 \nu_{ii} \frac{1}{r^2} \frac{\partial}{\partial r} \left[ r^3 n^2 \frac{\partial}{\partial r} \left( \frac{1}{rn} \frac{\partial n}{\partial r} \right) \right] \tag{6}$$

Using quasineutrality $\nabla \cdot \vec{\Gamma}^e = \nabla \cdot \vec{\Gamma}^i$ gives:

$$\begin{aligned} &\frac{d}{dz} \left\{ -\frac{en_0}{m_e \nu_{ei}^{(0)}} E_z - \frac{n_0 T}{m_e \nu_{ei}^{(0)}} \frac{1}{n} \frac{dn}{dz} \right\} \\ &\qquad = \frac{3 r_L^4 \nu_{ii}^{(0)}}{8 n_0} \frac{1}{r} \frac{\partial}{\partial r} \left\{ \frac{1}{r} \frac{\partial}{\partial r} \left[ r^3 n^2 \frac{\partial}{\partial r} \left( \frac{1}{rn} \frac{\partial n}{\partial r} \right) \right] \right\} \end{aligned} \tag{7}$$

For a given density profile, the potential can be determined by calculating $E_z$ and integrating along $z$. A precise calculation of the potential profile requires detailed knowledge of the density profile (accurate for four

derivatives). However, by letting $\partial/\partial r \propto 1/r_p$, and $\partial/\partial z \propto 1/L$ (and using $\nu_{ii} \propto \nu_{ei} \propto n$), the scaling of the radial dependence of $E_z$ is $E_z \propto n^2/r_p^4$ . Since the potential $\phi$ is an integral along $z$ of $E_z$, we also have $\phi \propto n^2/r_p^4$ . If initially the plasma expands radially without particle loss, then $n \propto r_p^{-2}$ and $\phi \propto n^4$ .

In the sharp-boundary limit, the $m = 1$ instability has a dipole charge distribution. This results in a uniform electric field $\mathbf{E}_1$ across the plasma, so that the plasma moves almost rigidly. We assume that the diffuse-boundary ballooning mode will also have a rigid radial profile because of FLR effects [6].

As the plasma position $\mathbf{r}_0 = (x_0, y_0)$ moves inside the stainless steel chamber, image charges hold the potential fixed near the conducting wall. Therefore the shape of the radial potential profile changes as the plasma moves. This behavior is approximated by assuming that, as the plasma moves off-center, the change in potential at a fixed point is less than the change due simply to translation of the profile by a factor $(1 - r^2/r_w^2)$, where $r_w$ is the wall radius. If the initially centered profile is parabolic:

$$\phi_i(r) = \phi_0 + \sigma r^2 \tag{8}$$

then the change of potential at a fixed $r$ due to plasma motion is:

$$\Delta\phi(r) = \left(1 - \frac{r^2}{r_w^2}\right) \sigma \left(|\mathbf{r} - \mathbf{r}_0|^2 - r^2\right) \tag{9}$$

Summing the initially centered potential profile, the change due to translation, and the instability potential $-\mathbf{E}_1 \cdot \mathbf{r}$ gives:

$$\phi(r) = \phi_0 + \sigma r^2 + \left(1 - \frac{r^2}{r_w^2}\right) \sigma \left(|\mathbf{r} - \mathbf{r}_0|^2 - r^2\right) - \mathbf{E}_1 \cdot \mathbf{r} \tag{10}$$

Using eight probes arrayed as in Figure 14, and labelling the potentials at each point by $\phi_1$, $\phi_2$,..., the equations above can be solved to give the $m = 1$ electric field independent of $\phi_i$:

$$E_{1x} = \left(\frac{r_w^2 - r_1^2}{r_2^2 - r_1^2}\right)\left(\frac{\phi_7 - \phi_5}{2r_2}\right) - \left(\frac{r_w^2 - r_2^2}{r_2^2 - r_1^2}\right)\left(\frac{\phi_3 - \phi_1}{2r_1}\right)$$
$$E_{1y} = \left(\frac{r_w^2 - r_1^2}{r_2^2 - r_1^2}\right)\left(\frac{\phi_8 - \phi_6}{2r_2}\right) - \left(\frac{r_w^2 - r_2^2}{r_2^2 - r_1^2}\right)\left(\frac{\phi_4 - \phi_2}{2r_1}\right) \tag{11}$$

Note that if no wall were present we would expect:

$$\phi(r) = \phi_0 + \sigma|\mathbf{r} - \mathbf{r_0}|^2 - \mathbf{E}_1 \cdot \mathbf{r} \tag{12}$$

In this case the plasma displacement $r_0$ cannot be eleminated from the equations for $\phi_1$, $\phi_2$, ..., $\phi_8$ because of the degeneracies $(\phi_7 - \phi_5)/r_2 = (\phi_3 - \phi_1)/r_1$ and $(\phi_8 - \phi_6)/r_2 = (\phi_4 - \phi_2)/r_1$ . The electric fields from Equation 11 are used to calculate $\mathbf{E} \times \mathbf{B}$ drifts which are compared with the plasma motion calculated from Langmuir probe ion saturation current measurements.

Figure 15 shows the time evolution of the ambipolar potential radial distribution for a stable shot. Measurement of the potential difference between probes at $x = -1.0$ and $x = 0.0$ cm as a function of density reveals a dependence $V \propto n^4$ early in time, when radial diffusion is the dominant loss mechanism. Later, as axial loss becomes more important, the dependence of floating potential on density is weakened. This behavior, which is observed consistently, confirms our model of a uniform-temperature plasma. The measurements used to determine the electric field are made at small radii ($r \leq 2.0$ cm) where the profile can be approximated by a parabola.

Figure 16 shows the radial potential profile along $\hat{x}$ for a flute-unstable plasma. In this case, the instability has produced an electric field in the $-\hat{x}$ direction, resulting in an $\mathbf{E} \times \mathbf{B}$ drift in the $-\hat{y}$ direction ($\mathbf{B}$ is in the $-\hat{z}$ direction). Similar results are obtained for plasmas with ballooning behavior.

# C Measurement of Perturbed Magnetic Fields

Ballooning modes are characterized by axial variation of the mode amplitude. In ideal MHD, the magnetic field lines move and bend with the plasma, giving rise to a perturbed magnetic field $\tilde{\mathbf{B}}$ which is perpendicular to $\mathbf{B_0}$ . For a background field $\mathbf{B_0} = 2$ kG which is bent $\sim 2$ cm over a length 100 cm, the perturbed magnetic field will be $\tilde{\mathbf{B}} \sim 40$ Gauss. The components of this field can be measured and distinguished from the azimuthally symmetric background field using compensated magnetic probes placed 180° apart.

The voltage induced in a magnetic probe with $N$ loops of area $A$ by a time-varying $\mathbf{B}$ field is:

$$V = -NA\frac{\partial B_\perp}{\partial t} \tag{13}$$

Each magnetic probe consists of 80 turns of wire at an average diameter of 0.106 cm with a length of 0.5 cm. The calculated inductance is $L = 1.4\ \mu$H, and is in agreement with measurements made on a Tektronix Type 130 L-C meter. The probes were calibrated by measuring the voltage induced when placed in a solenoid with an oscillating magnetic field and using the

relationship:

$$NA = \left| \frac{V}{\omega B} \right| \tag{14}$$

The resulting calibration for the two probes used are:

$$\begin{aligned} (NA)_1 &= 0.59 \text{ turns} \cdot \text{cm}^2 \\ (NA)_2 &= 0.57 \text{ turns} \cdot \text{cm}^2 \end{aligned} \tag{15}$$

To compensate for the different probe calibrations, a voltage divider is used to decrease the signal from probe #1:

$$\frac{R_2}{R_1 + R_2} = \frac{0.57}{0.59} \tag{16}$$

For $R_2 = 78\ \Omega$, this gives $R_1 = 2.7\ \Omega$, which is the value used in Figures 4 and 5 .

# D Beta-dependence of growth rate

The exponent in the expression $\ln \xi = a + b\langle\beta\rangle^{\alpha}$ was determined by testing the quality of a linear fit for various values of alpha using the points shown in Figure 8 except for two points which lie far above the line.

The method used is an F-test, which tests the probability that the coefficient of a quadratic term $c\langle\beta\rangle^{2\alpha}$ is zero. A plot of this probability $P(c = 0)$ versus $\alpha$ is given in Figure 17 .

We see that at $\alpha = 0.44$, the probability that the straight line is the correct polynomial fit is $P(c = 0) = 0.94$ . Using the level where $P(c = 0)$ drops by one half of its maximum value as a measure of acceptable error, we get $\alpha = 0.44 \pm 0.16$ . This is within a standard deviation of the theoretical expectation of $\alpha \approx 0.50$ .

# References


[1] H.D. Price, N.M.P. Benjamin, B.K. Kang, A.J. Lichtenberg, M.A. Lieberman, Phys. Fluids 28, 392 (1985).

[2] H.D. Price, *Confinement and Stability of a Plasma in Multiple Magnetic Mirrors*, PhD Thesis, University of California, Berkeley, 1982.

[3] R.J. Commisso, C.A. Ekdahl, K.B. Freese, K.F. McKenna, and W.E. Quinn, **Phys. Rev. Lett. 39**, 137 (1977).

[4] J.P. Freidberg, L.D. Pearlstein, **Phys. Fluids 21**, 1207 (1978).

[5] R. Hatakeyama, N. Sato, M. Inutake, **Nucl. Fusion 23**, 1467 (1983).

[6] T.B. Kaiser, L.D. Pearlstein, **Phys. Fluids 28**, 1003 (1985).

[7] B.K. Kang, *MHD Stability and Control for Mirror Machines*, PhD Thesis, University of California, Berkeley, 1986.

[8] X.S. Lee, P.S. Catto, **Phys. Fluids 24**, 2010 (1981).

[9] M.Tuszewski, D. Price, M.A. Lieberman, R. Bravenec, K. Doniger, C. Hartman, A.J. Lichtenberg, **Nucl. Fusion 19**, 1244 (1979).

[10] R.V. Bravenec, *Axial Flow of a Collisional Plasma Through Multiple Magnetic Mirrors*, PhD Thesis, University of California, Berkeley 1982.

[11] J. Marshall, **Phys. Fluids 3**, 135 (1960).

[12] M. Tuszewski, A.J. Lichtenberg, **Phys. Fluids 20**, 1263 (1977).

## Acknowledgements

Thanks to M.A. Lieberman and C.W. Hartman for many contributions to this work. Special gratitude is due B.K. Kang for his theoretical contributions. Thanks to H. Meuth for assistance on many aspects of the experiments, and to B. Bingham and J. Benasso for excellent technical support. The authors are grateful to H.D. Price for help in the early stages of the experiments. This work was supported by DOE Contract No. DE-AS03-76ET53059 and DOE Grant No. DE-FG03-85ER51103.

## Figure captions

1. The Berkeley Multiple Mirror Experiment (top) and axial magnetic field profile (bottom).

2. Centroid motion for a ballooning plasma instability (1) in a mirror cell and (2) near a stabilizing magnetic cusp calculated using data from four Langmuir probes.

3. Velocity calculated from Langmuir probe array ion saturation current measurements (light trace) and floating probe array measurements (dark trace) for a flute-unstable configuration.

4. Perturbed magnetic field (dark) and plasma $x$-position (light) versus time for a flute mode.

5. Perturbed magnetic field (dark) and plasma $x$-position (light) versus time for a plasma stabilized against flute modes (ballooning).

6. Resistive growth rate versus beta for $N_c = 1$, $\tau_R = 43$ $\mu$sec.

7. Resistive growth rate versus mirror ratio for $N_c = 1$, $p_m/p_c = 2$, $\tau_R = 43$ $\mu$sec.

8. Plot of $\ln \xi$ versus $\langle\beta\rangle^{1/2}$ for $N_c = 1$, $R_m \geq 3.0$, and $1.0 \leq p_m/p_c \leq 3.0$. $\xi$ is normalized to 1 cm.

9. Plot of $\xi$ versus $R_m$ for $N_c = 1$, $0.068 \leq \langle\beta\rangle \leq 0.108$, and $1.0 \leq p_m/p_c \leq 3.0$ .

10. Plot of $\ln\xi$ versus $\gamma_T$ for $N_c = 1$ and $1.0 \leq p_m/p_c \leq 3.0$ .

11. Plot of $\ln\xi$ versus $\langle\beta\rangle^{1/2}$ for $N_c = 3$, $R_m \geq 3.0$, and $1.0 \leq p_m/p_c \leq 3.0$ .

12. Plot of $\ln\xi$ versus $R_m$ for $N_c = 3$, $0.017 \leq \langle\beta\rangle \leq 0.041$, and $1.0 \leq p_m/p_c \leq 4.0$ .

13. Plot of $\ln\xi$ versus $\gamma_T$ for $N_c = 3$ and $1.0 \leq p_m/p_c \leq 3.0$ .

14. Arrangement of 8 electric probes. Typically $r_1 = 1.5$ cm and $r_2 = 2.5$ cm.

15. Floating potential profile for a stable shot.

16. Floating potential profile for an unstable shot.

17. Probability of zero quadratic coefficient versus exponent $\alpha$ for the experimental fit $\ln\xi = a + b\langle\beta\rangle^{\alpha} + c\langle\beta\rangle^{2\alpha}$ .

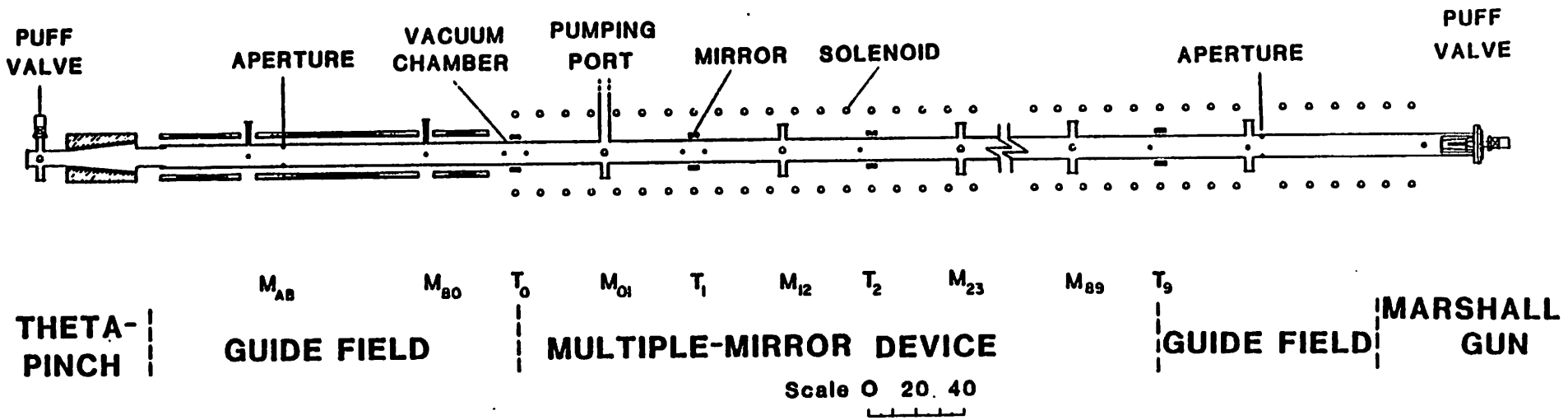
PUFF VALVE
APERTURE
VACUUM CHAMBER
PUMPING PORT
MIRROR
SOLENOID
APERTURE
PUFF VALVE
$M_{AB}$
$M_{BO}$
$T_0$
$M_{01}$
$T_1$
$M_{12}$
$T_2$
$M_{23}$
$M_{89}$
$T_9$
THETA-PINCH
GUIDE FIELD
MULTIPLE-MIRROR DEVICE
GUIDE FIELD
MARSHALL GUN
Scale 0 20 40

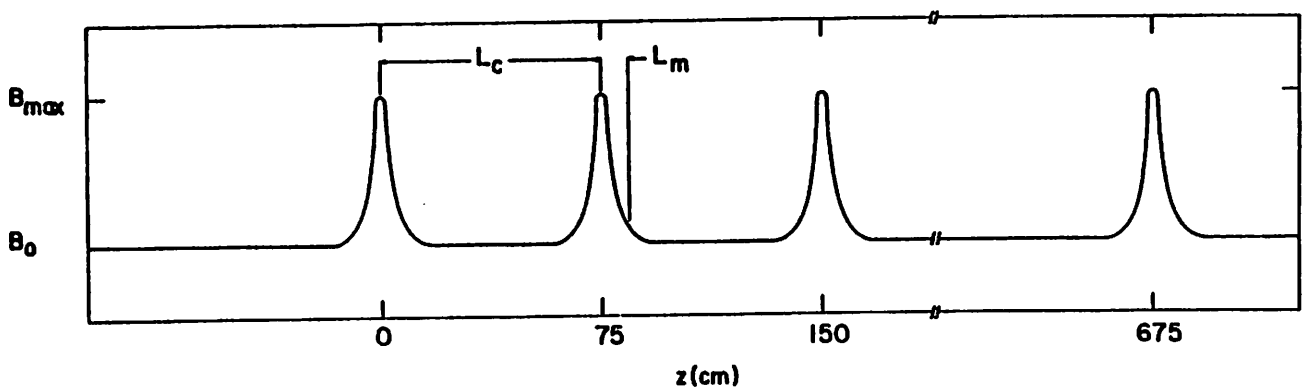
$B_{max}$
$B_0$
$L_c$
$L_m$
0
75
150
675
z(cm)

Figure 1

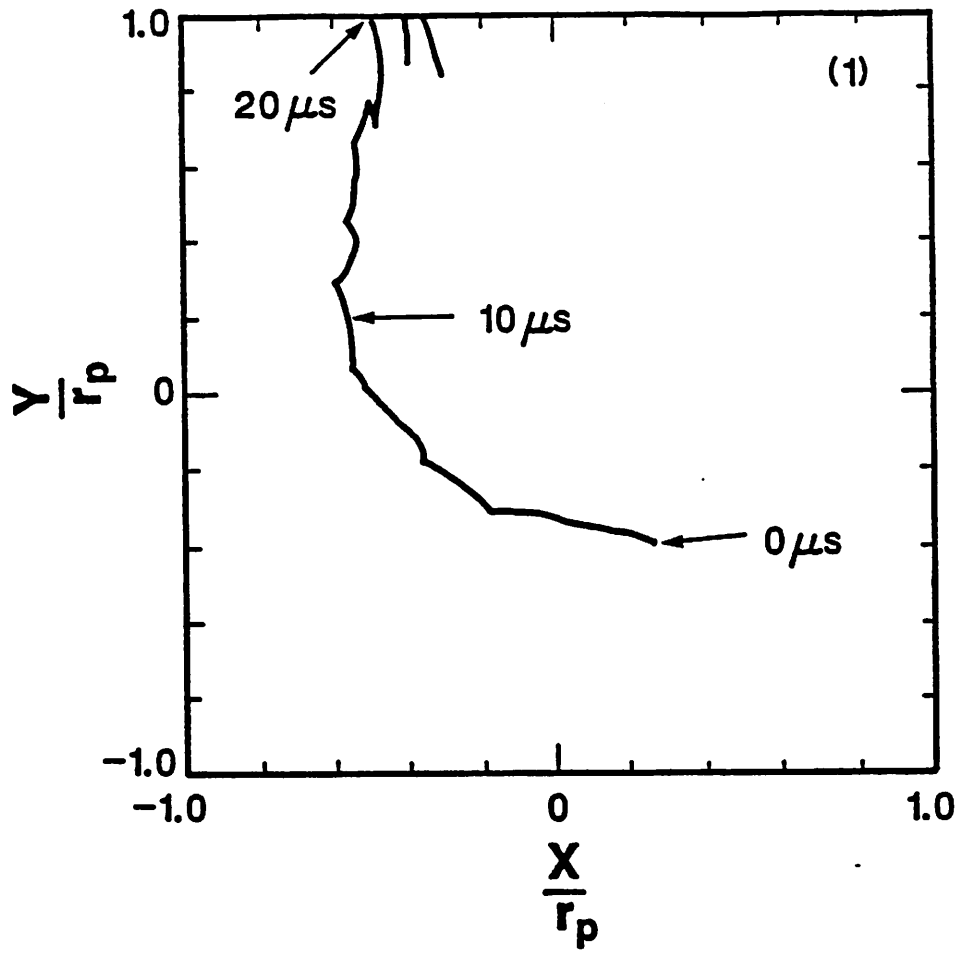
1.0
(1)
20 μs
10 μs
0 μs
Y/rp
0
-1.0
-1.0
0
1.0
X/rp

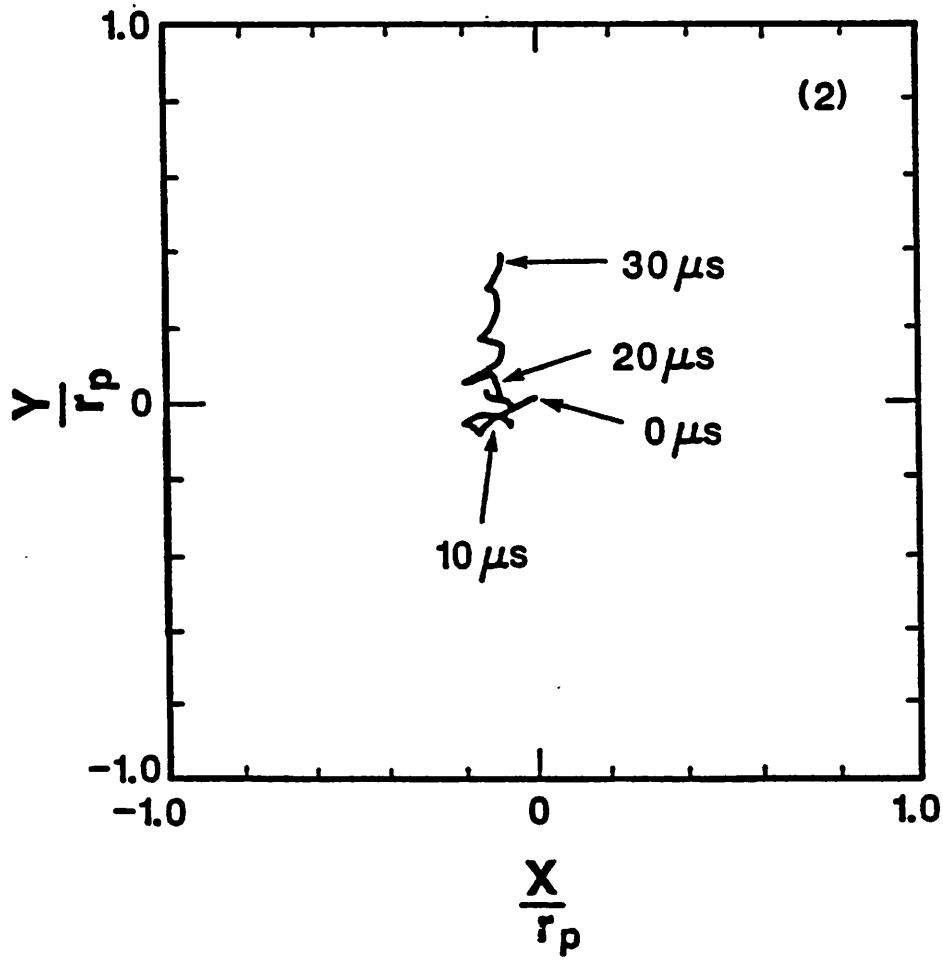
1.0
(2)
30 μs
20 μs
0 μs
10 μs
Y/rp
0
-1.0
-1.0
0
1.0
X/rp

Figure 2

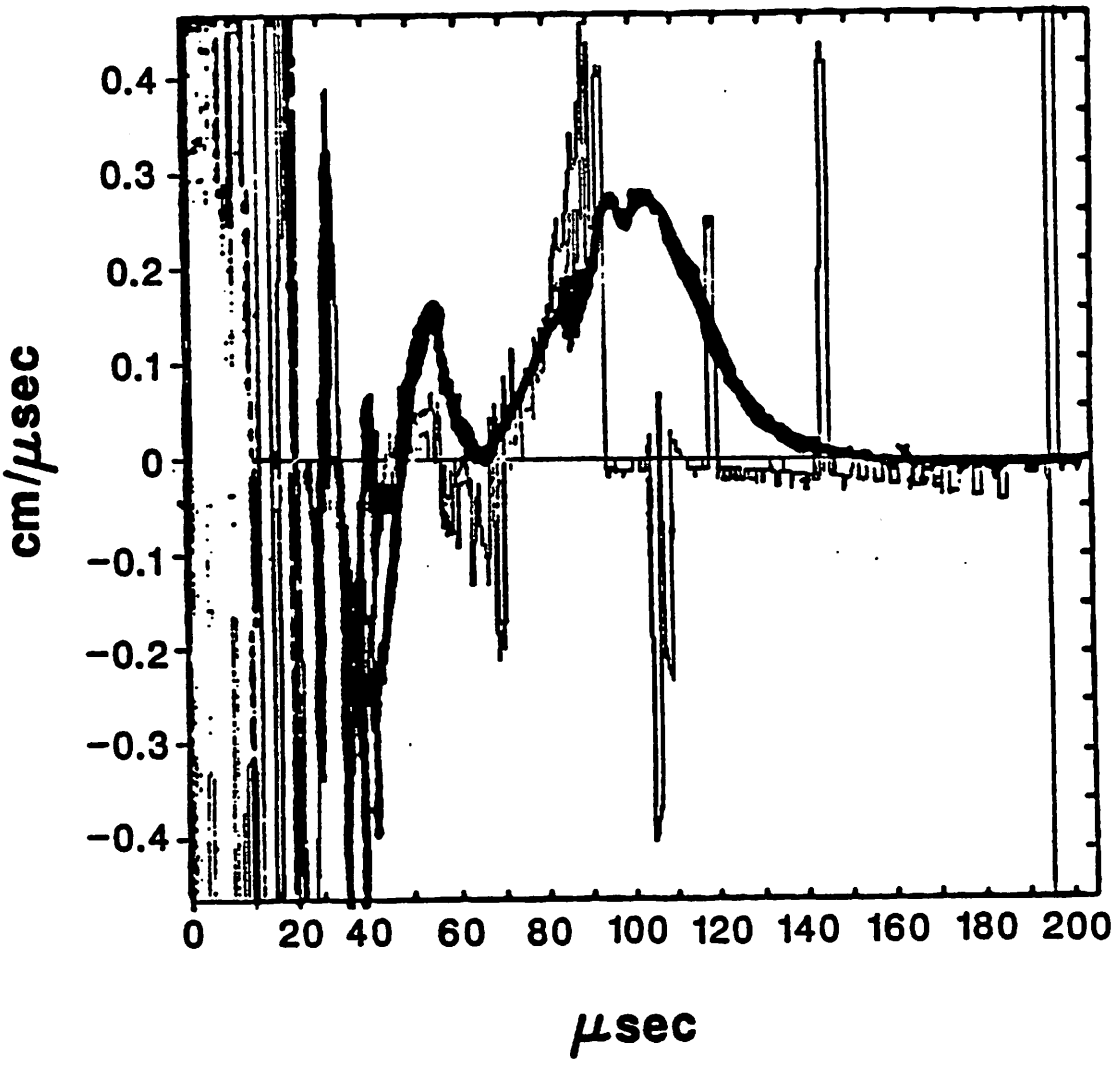
0.4
0.3
0.2
0.1
0
-0.1
-0.2
-0.3
-0.4
cm/μsec
0
20
40
60
80
100
120
140
160
180
200
μsec

Figure 3

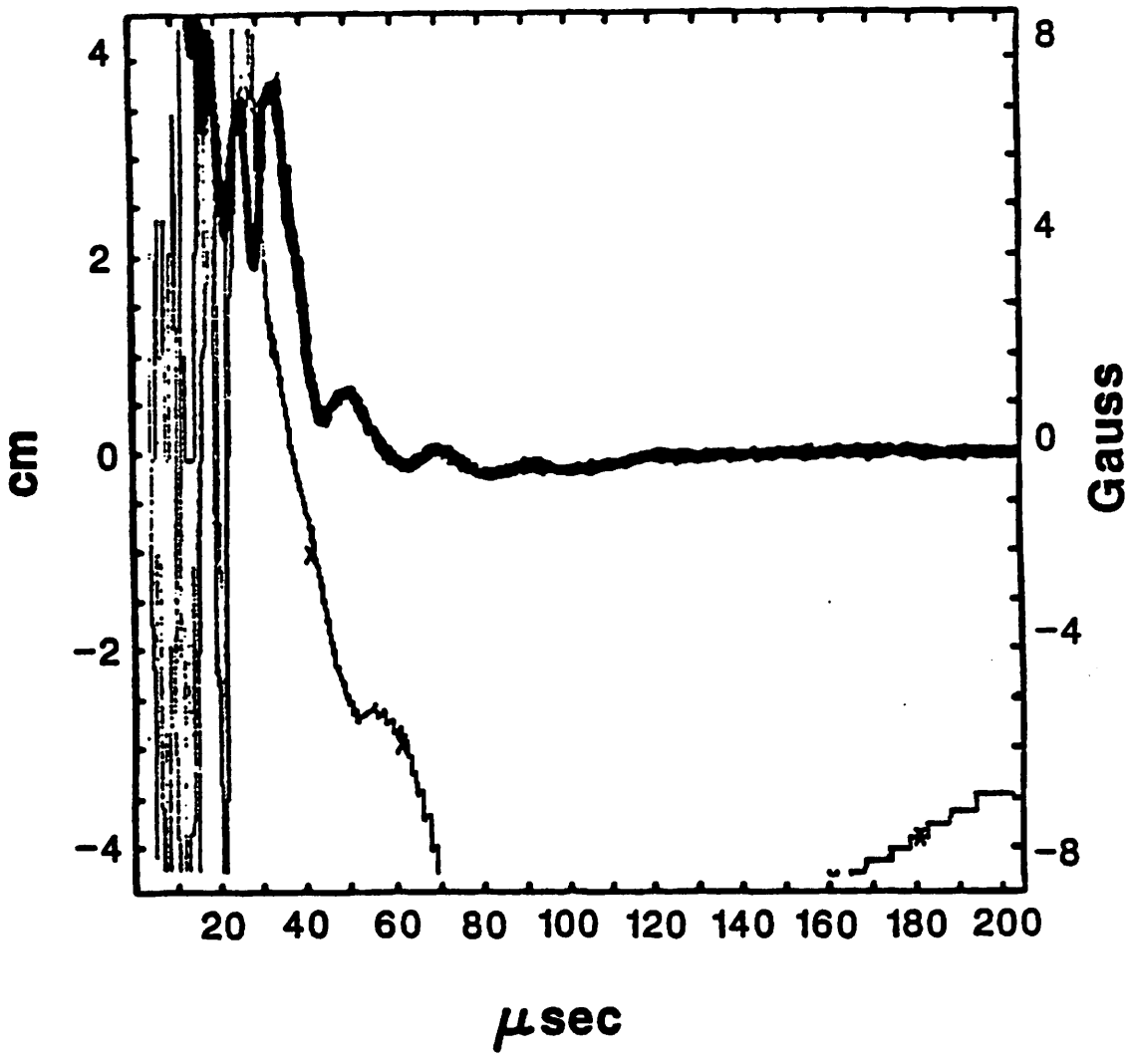


Figure 4

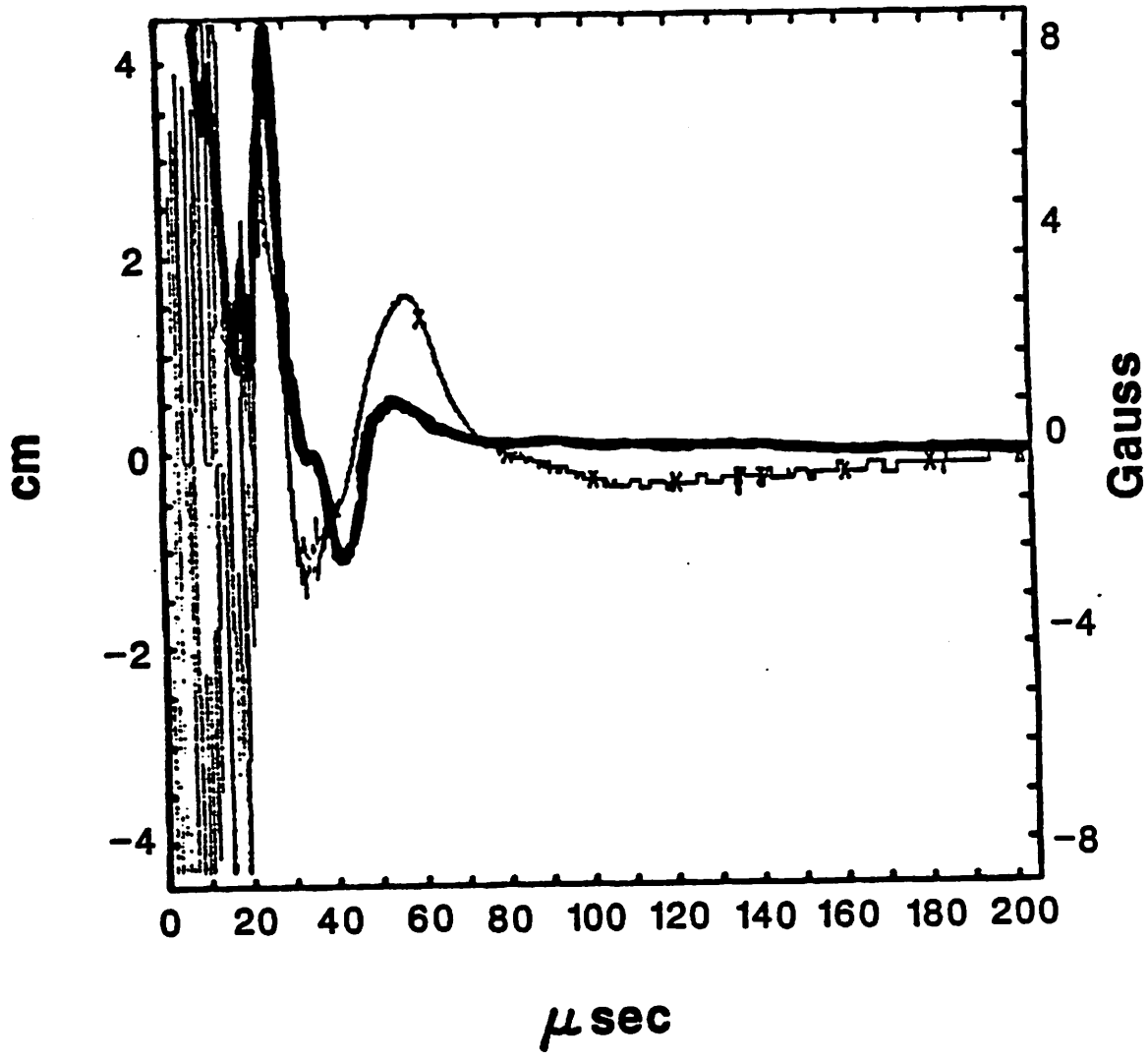


Figure 5

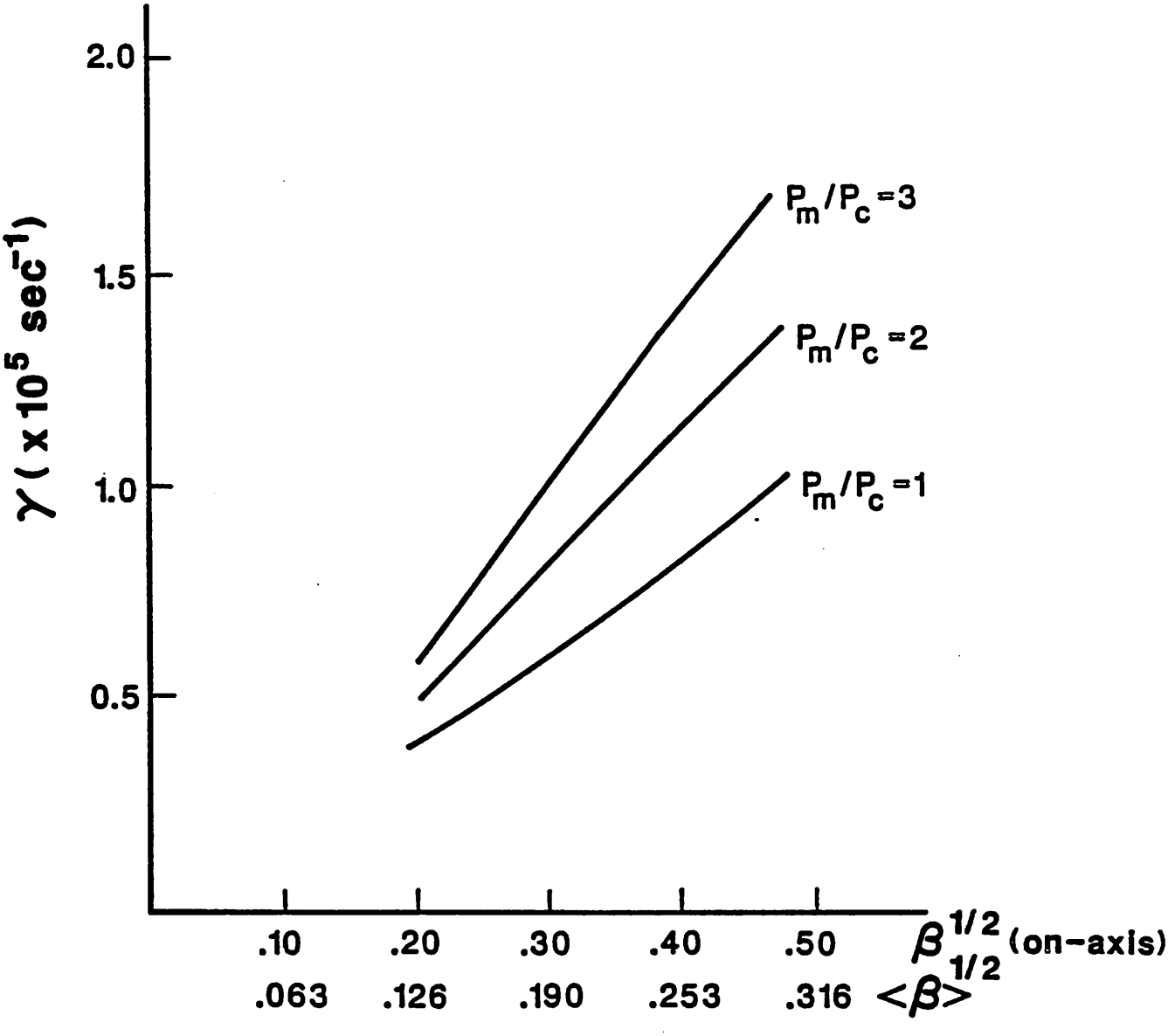
2.0
1.5
1.0
0.5
$\gamma$ ( x $10^5$ $sec^{-1}$)
$P_m/P_c$ =3
$P_m/P_c$ =2
$P_m/P_c$ =1
.10
.20
.30
.40
.50
$\beta^{1/2}$ (on-axis)
.063
.126
.190
.253
.316
$\langle\beta\rangle^{1/2}$

Figure 6

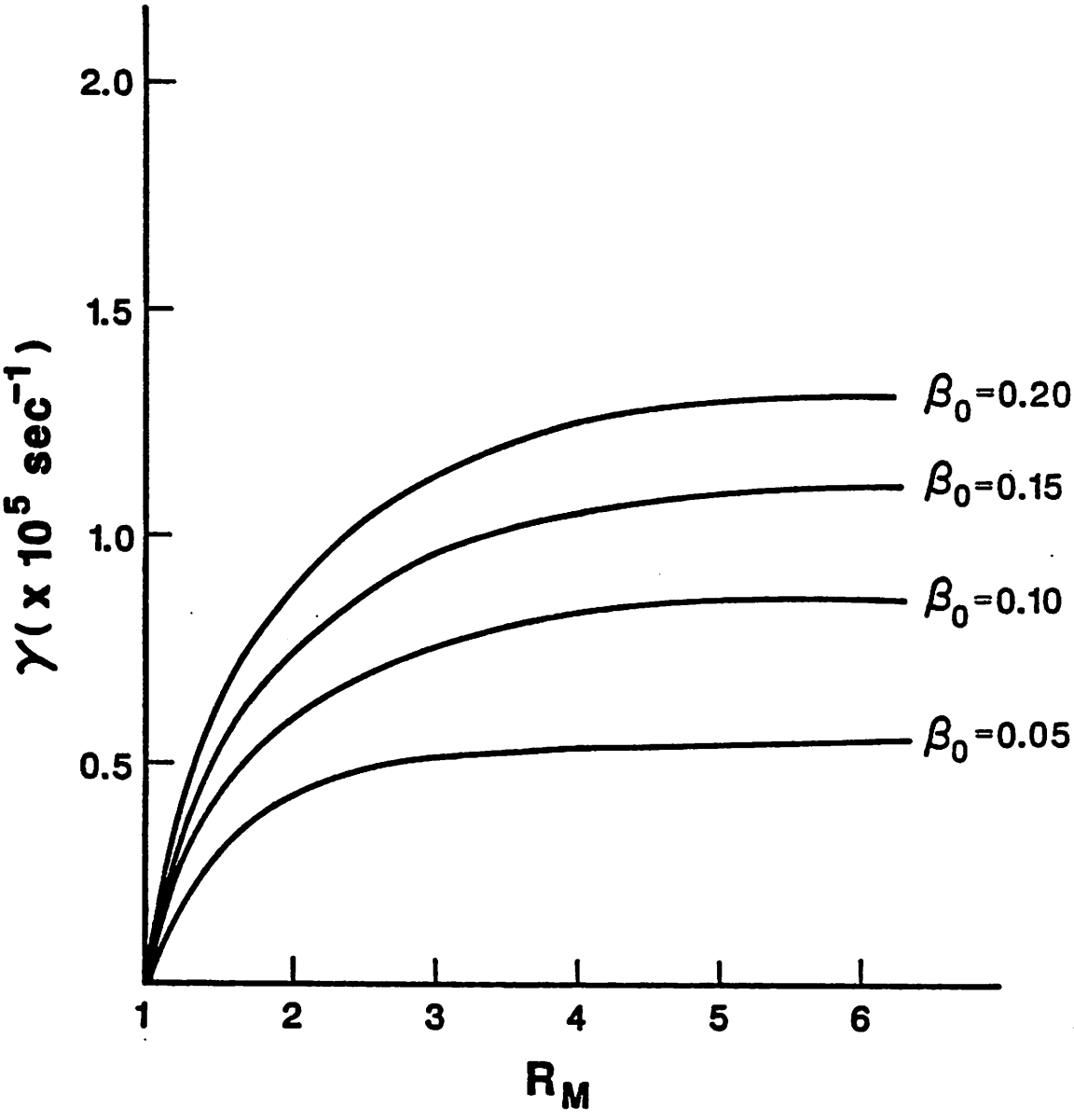


Figure 7

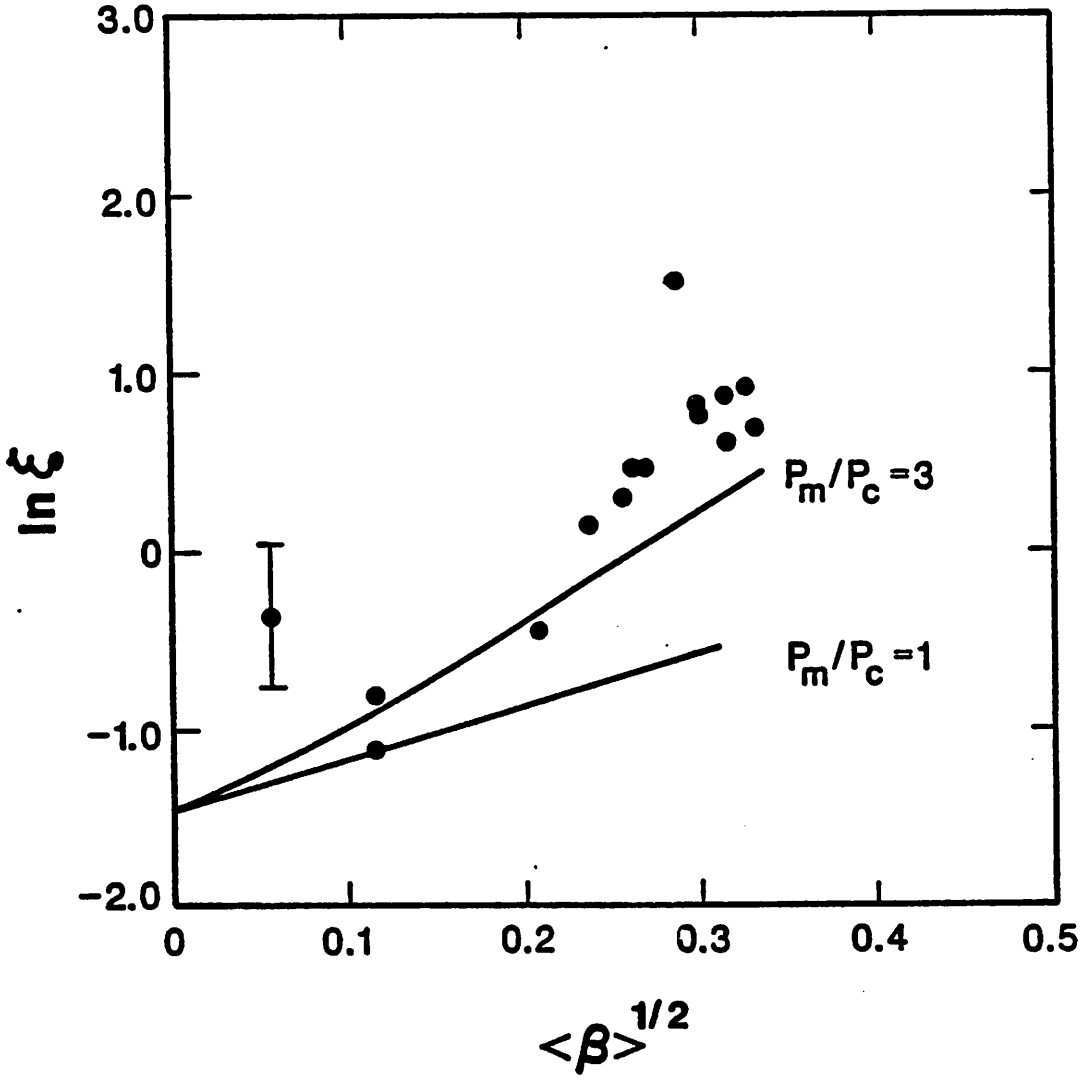
3.0
2.0
1.0
0
-1.0
-2.0
0
0.1
0.2
0.3
0.4
0.5
ln ε
$P_m/P_c$ =3
$P_m/P_c$ =1
$\langle\beta\rangle^{1/2}$

Figure 8

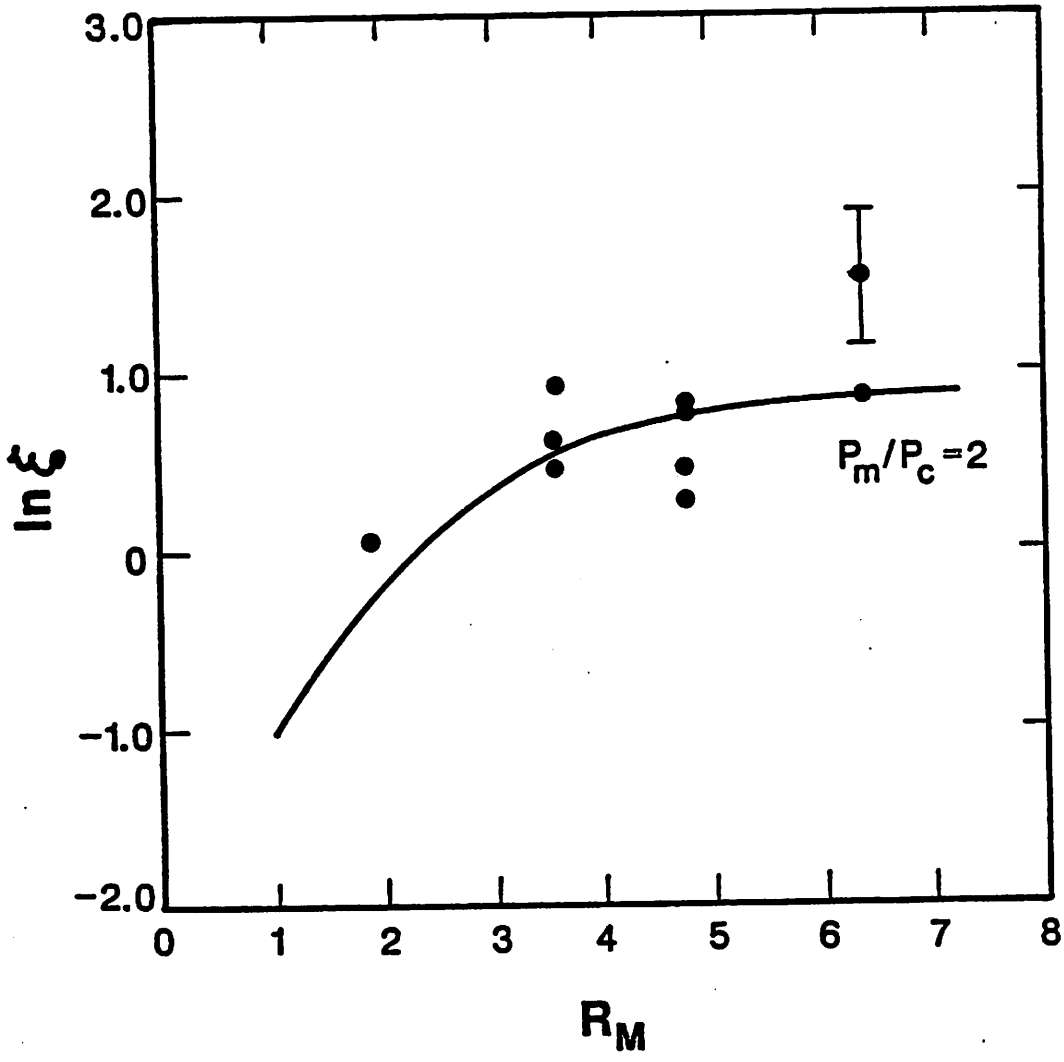


Figure 9

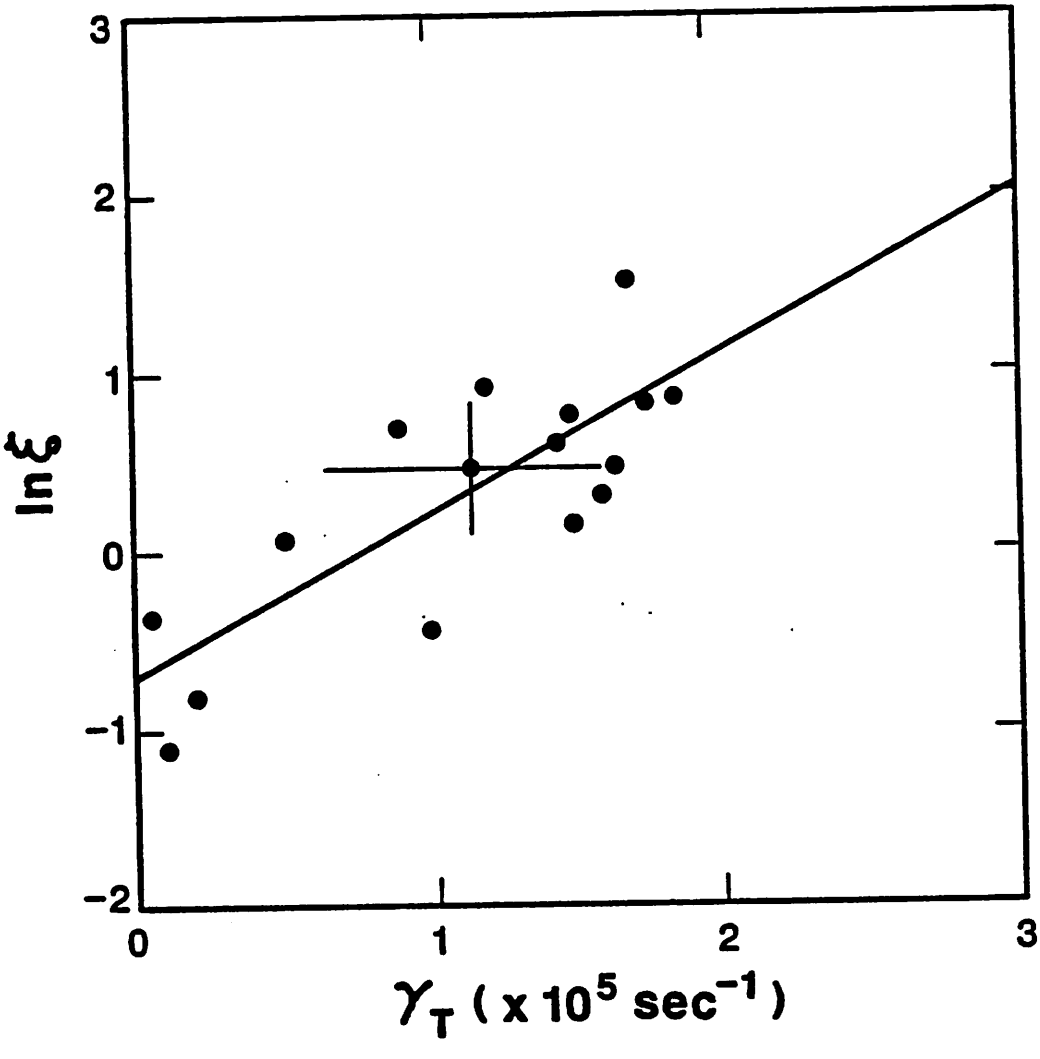


Figure 10

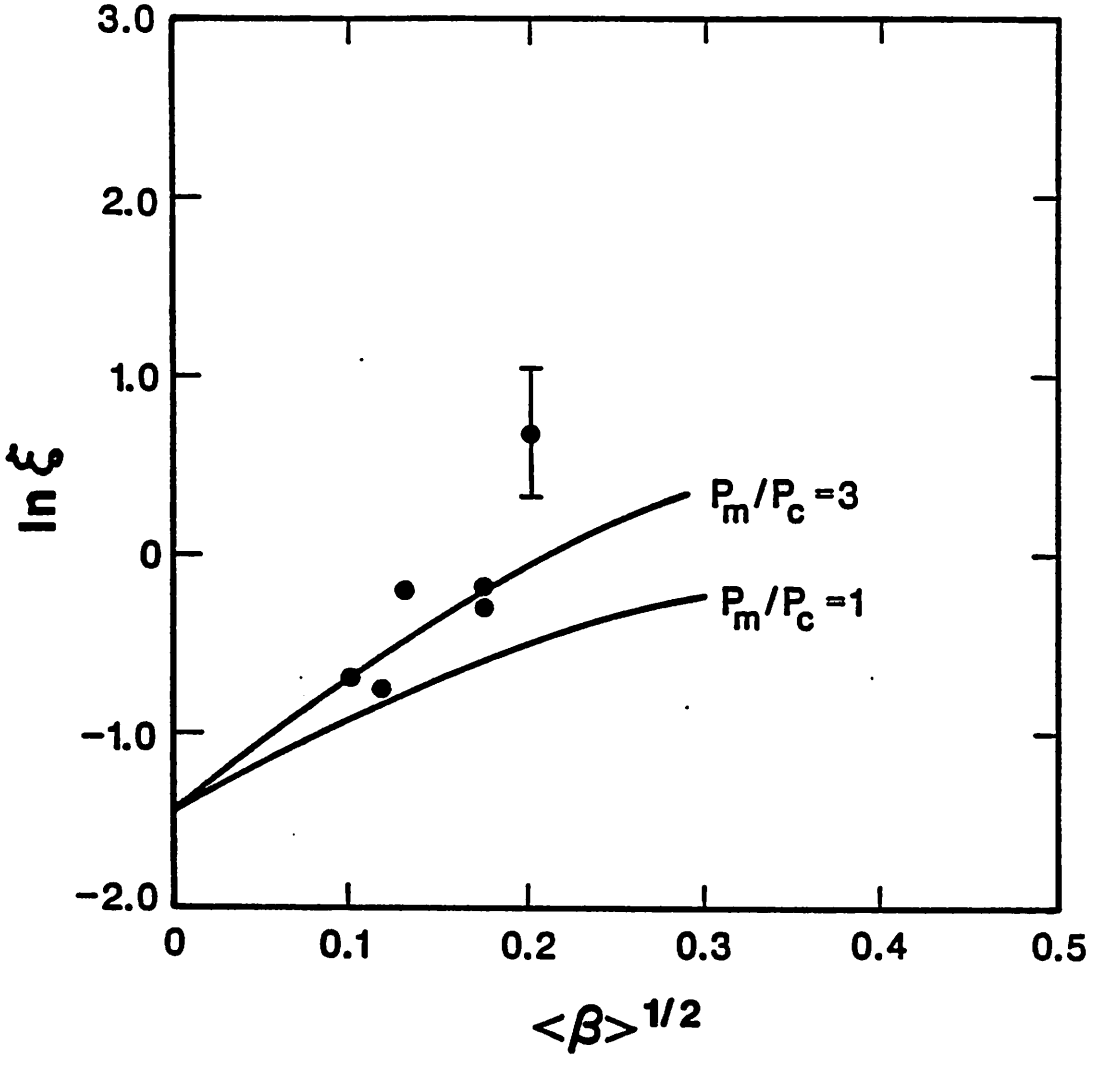
3.0
2.0
1.0
0
-1.0
-2.0
0
0.1
0.2
0.3
0.4
0.5
ln ξ
$P_m/P_c$ =3
$P_m/P_c$ =1
$\langle\beta\rangle^{1/2}$

Figure 11

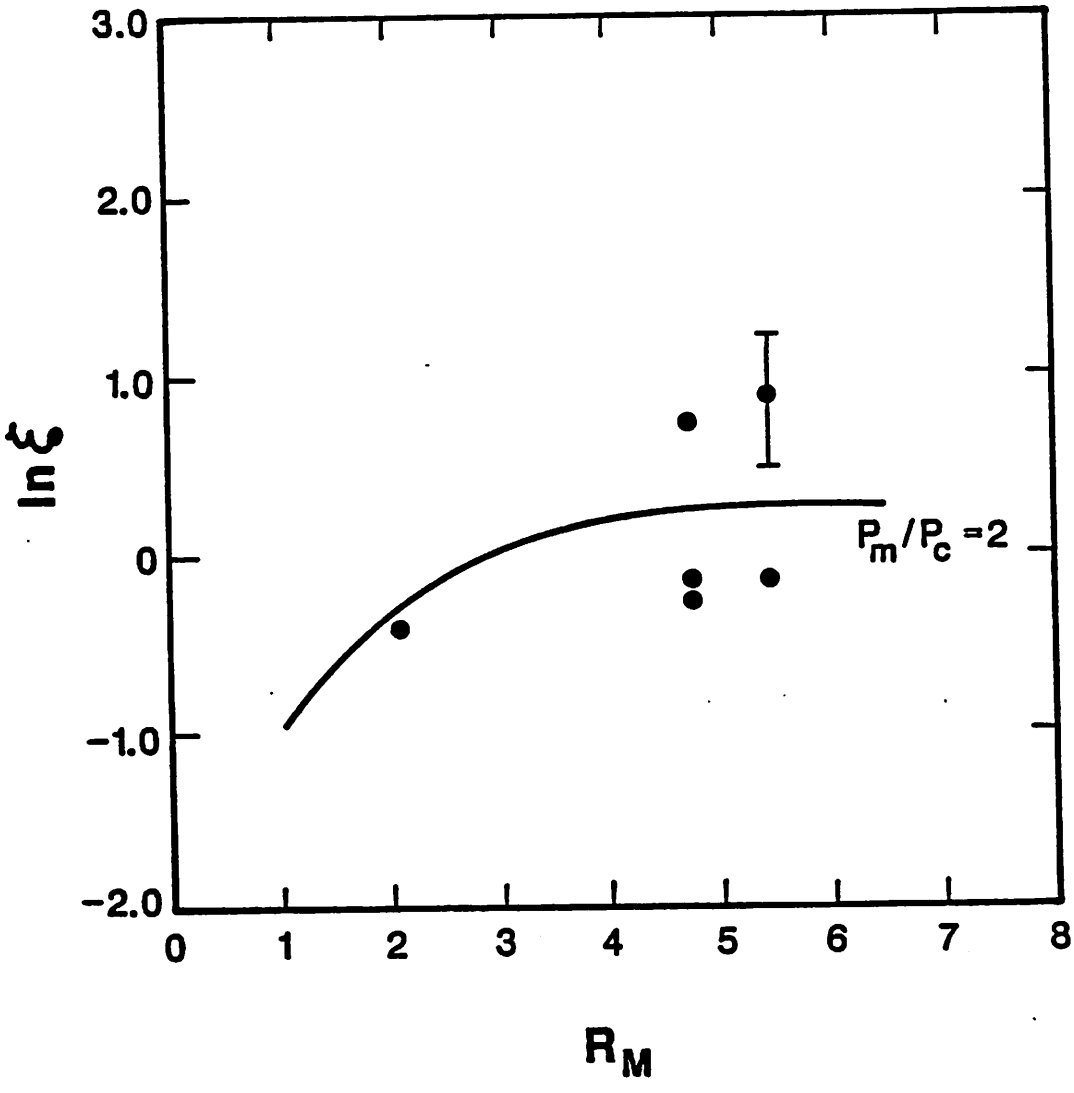


Figure 12

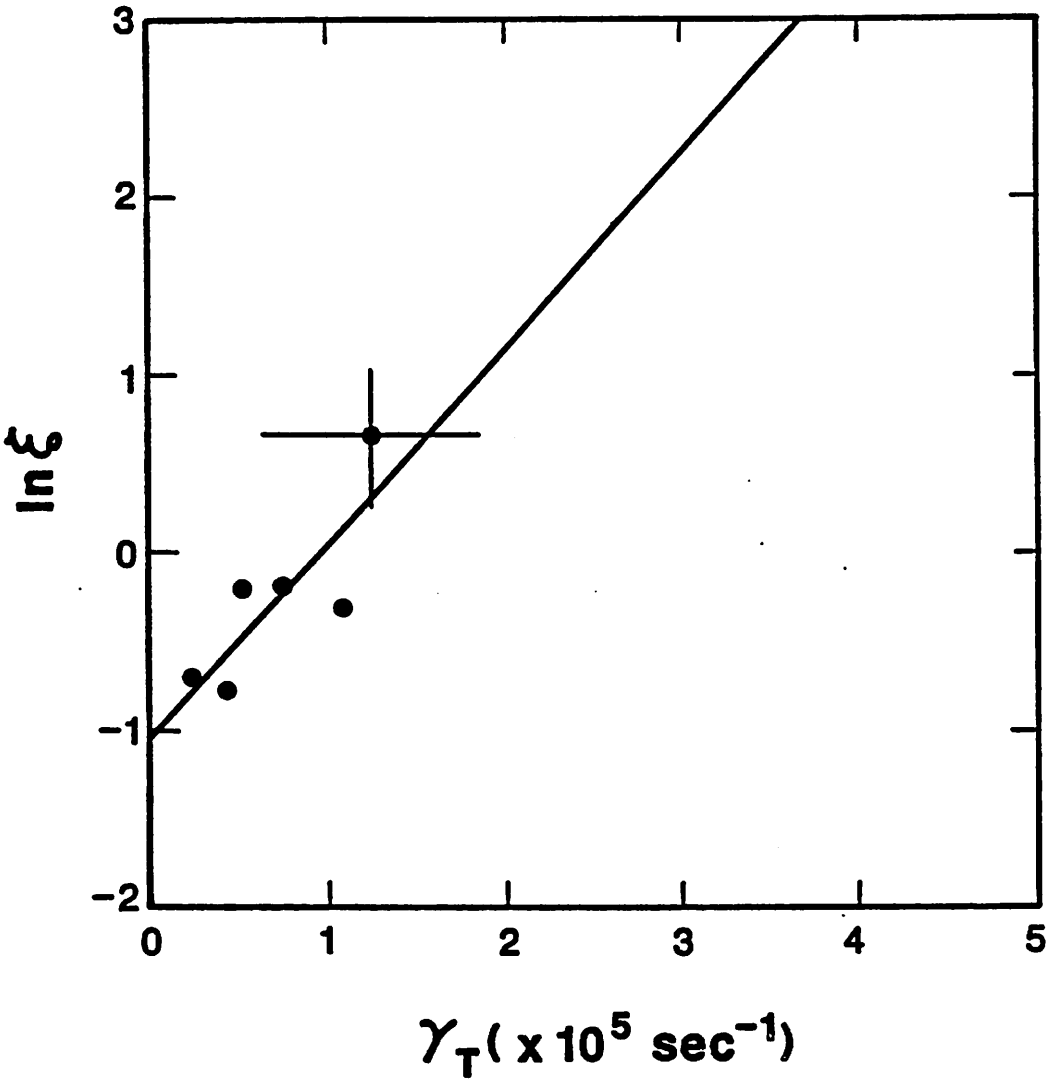


Figure 13

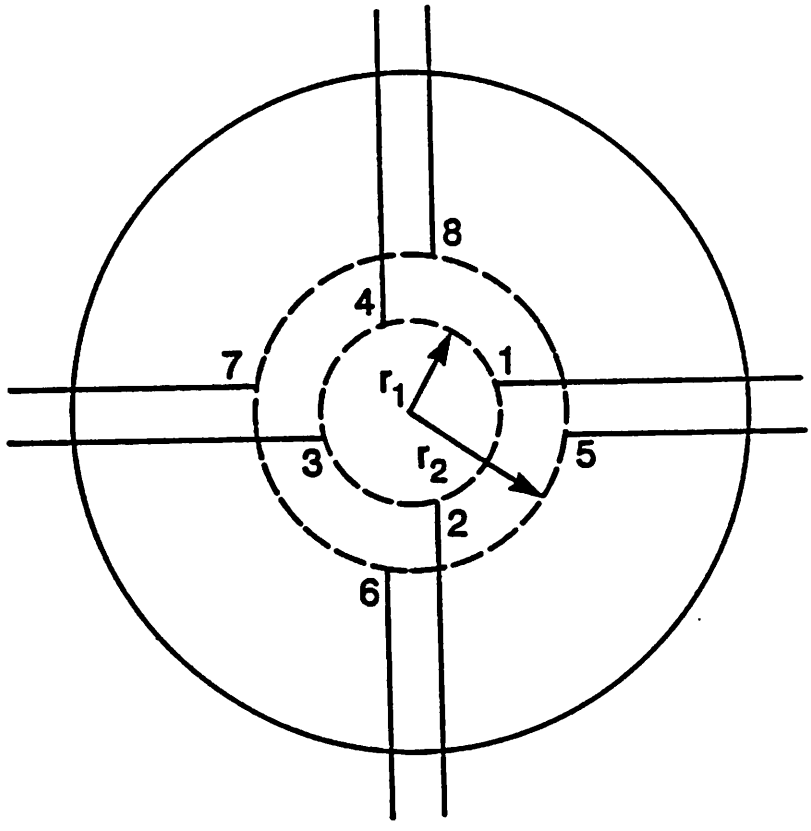


Figure 14

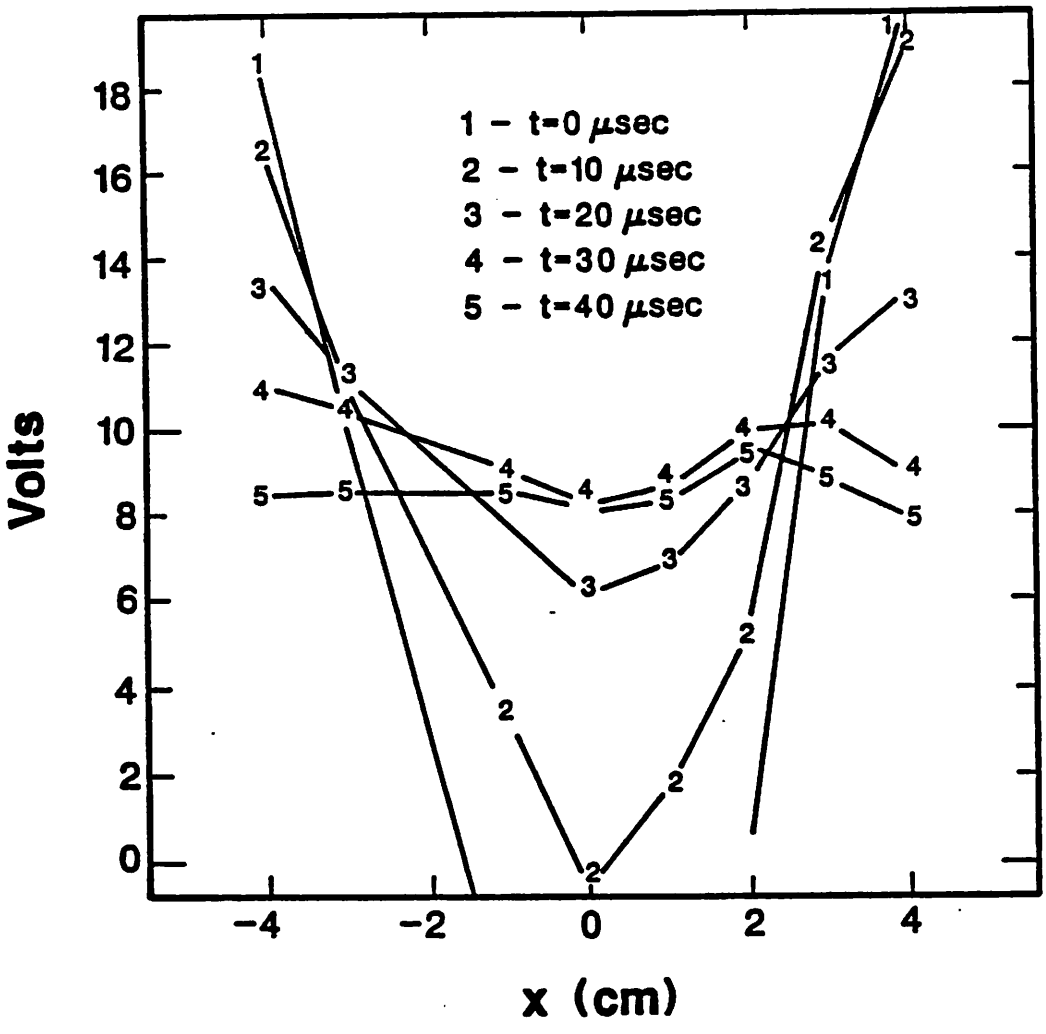
1 – t=0 μsec
2 – t=10 μsec
3 – t=20 μsec
4 – t=30 μsec
5 – t=40 μsec
Volts
x (cm)
18
16
14
12
10
8
6
4
2
0
−4
−2
0
2
4

Figure 15

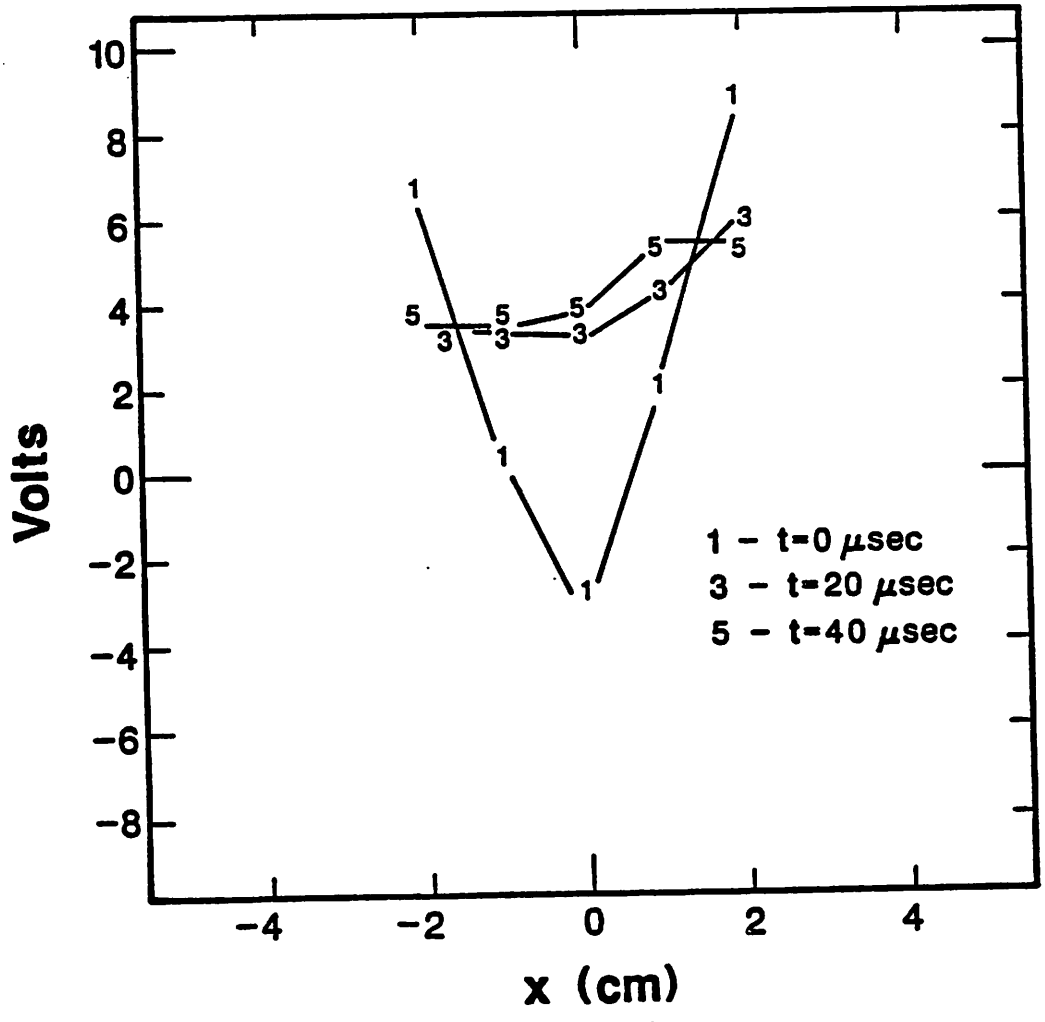


Figure 16

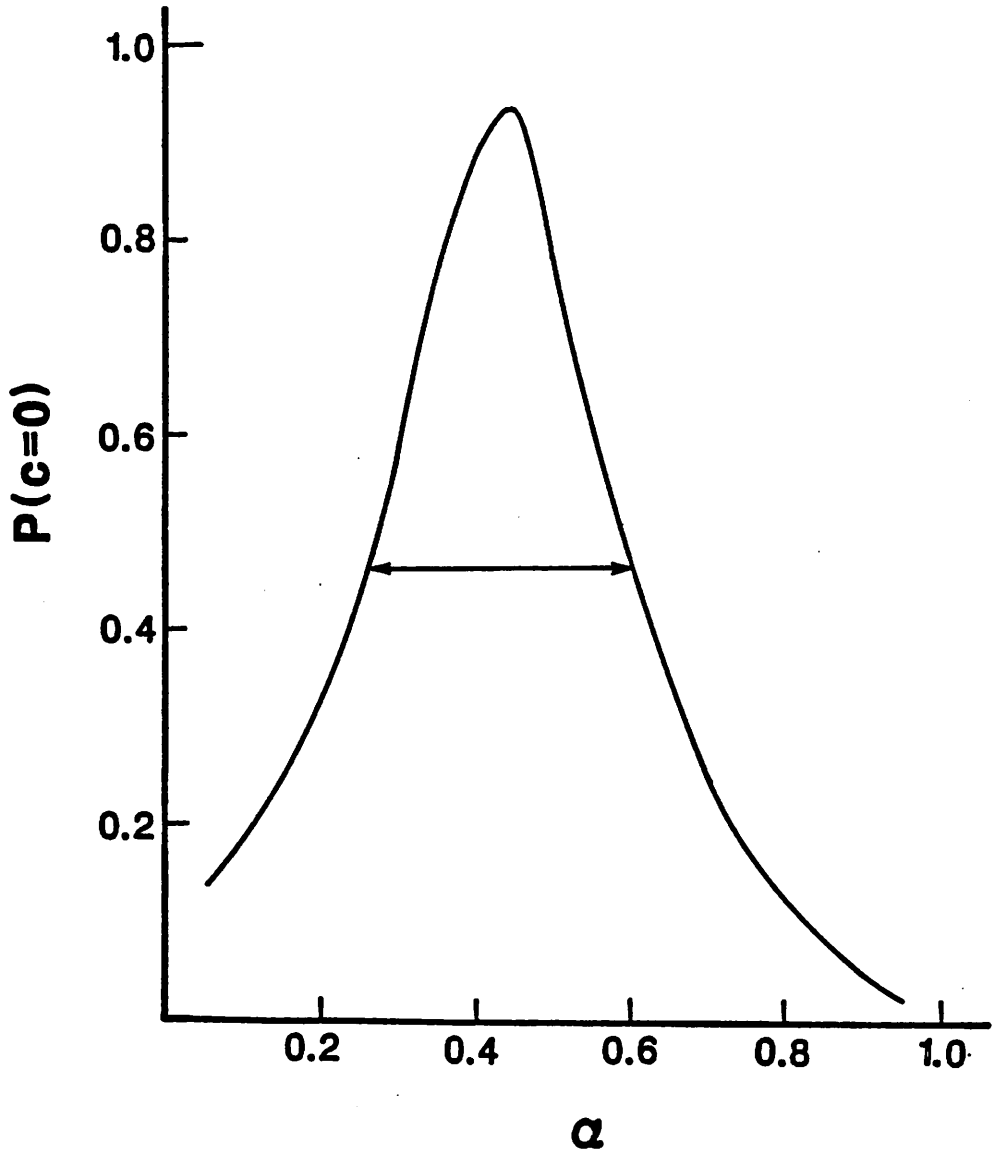


Figure 17